Influence of relevant parameters on the radial PIC simulation of a Hall effect thruster discharge

A. Domínguez-Vázquez[1], **F. Taccogna**[2], **P. Fajardo**[1], **E. Ahedo**[1]
[1]Equipo de Propulsión Espacial y Plasmas, Universidad Carlos III de Madrid, Leganés, Spain, addoming@ing.uc3m.es
[2]CNR-NANOTEC - PLasMI Lab, via Amendola 122/D, 70126 Bari, Italy, francesco.taccogna@nanotec.cnr.it.

KEYWORDS: Hall effect thrusters, particle-in-cell simulations, secondary electron emission

ABSTRACT:

An investigation on the influence of different parameteres on a Hall effect thruster plasma discharge is performed using a radial particle-in-cell model with secondary electron emission from the walls and a radial magnetic field. In particular, different field values, wall temperature and secondary electron emission are considered. Besides, a plane case (i.e. at larger radius) is explored. Primary and secondary electrons show different temperature anisotropy. Secondary electrons are found to be partially recollected at the walls and partially turned into primary electrons through collisional processes. Significant asymmetries at the inner and outer walls are found for the collected currents, the mean impact energy, and the wall and sheath potentials. Radial profiles in the plasma bulk are asymmetric too, due to a combination of the geometric expansion, the magnetic mirror effect, and the centrifugal force (emanating from the $E \times B$ drift). The asymmetries above vanish for the planar case, for which the temperature non-uniformity is the major responsible for the deviation from the classical Boltzmann relation on electrons along the magnetic lines.

1. INTRODUCTION

In a recent paper in the process now of being published [1] we considered a 1D radial particle-in-cell model of the plasma discharge at an axial section within the acceleration region of an annular Hall effect thruster (HET), assuming a radial magnetic field and significant secondary electron emission (SEE) by the lateral ceramic walls. The main goals of that work were to analyze the combined effects of SEE and cylindrical asymmetry on (a) the velocity distribution function (VDF) of ions and electrons (mainly on these ones) and (b) the macroscopic steady-state plasma response. The most valuable results of this work are:
- the radial profiles in both the plasma bulk and sheaths are asymmetric due to a combination of the geometric expansion, the magnetic mirror effect, and the centrifugal force (this last one emanating from the $E \times B$ drift);
- the collected electric currents, the mean impact energy, and the wall and sheath potentials present significant differences at the inner and outer walls;
- the two secondary electron populations are partially recollected by the walls and partially converted into primary electrons;
- the perpendicular and parallel temperatures to the magnetic field are different, and their ratios are different for primary and secondary electrons; and
- the temperature anisotropy and non-uniformity, and the centrifugal force modify the classical Boltzmann relation on electrons along the magnetic lines.
The model and the numerical code presented in Ref. [1] were based on the original ones by Taccogna [2], but we added two important improvements on numerical algorithms. The first one was to add a temporal control of the neutral density, $n_n(t)$, in order to have a prescribed mean plasma density, $\bar{n}_e$, thus assuring a steady-state discharge. The second one was to use a time-extended volumetric weighting algorithm that allows to obtain correct values of macroscopic variables of populations with very different densities; this was the case of the densities of secondary an primary electron populations.
The reader is invited to read Ref. [1] to get a full account of the model, the new numerical algorithms, and the results on the VDFs and the plasma macroscopic profiles. The paper illustrates them with a single simulation case. The purpose of the present work is to carry out a limited investigation of the influence of certain parameters on the results in order to get further insight on the physics of the response. Section 2 briefly summarizes the model and the code used. Section 3 discusses several cases, each one modifying one parameter from the reference case of Ref. [1]. Section 4 is for conclusions.
As pointed out already in Ref. [1], previous analytical work on this subject was carried out by Ahedo and Parra [3] and Ahedo and dePablo [4], while relevant numerical work is due to Sydorenko, Kaganovich, and coworkers [5, 6] and Taccogna et al. [2, 7, 8].

2. THE RADIAL MODEL

Figure 1 sketches the annular HET chamber with r_1 and r_2 as inner and outer radius. The 1D radial (1Dr) model selects a radial section near the chamber exit where the axial electric field is already signif-

icant and the plasma beam is already accelerating. The 1Dr model considers electrons e, (singly-charged) ions i, and neutrals n. Electrons and ions are modelled as two populations of macroparticles with densities and temperatures, n_j and T_j $(j = i, e)$, evolving with (r, t) from initial Maxwellian populations uniformly distributed along the radial domain with n_{j0} and T_{j0} $(j = i, e)$. Neutrals are modeled just as a spatially-uniform background with a constant temperature T_n and a time-dependent density $n_n(t)$. This one is adjusted by an ionization-controlled discharge (ICD) algorithm [1] in order that the mean electron density in domain, $\bar{n}_e$, remains constant (which is equivalent to keep constant the total amount of plasma in the domain). There is not axial contribution of plasma in this model.

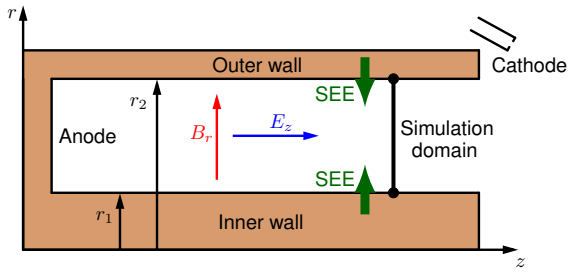

Figure 1: Sketch of a HET. The simulation domain corresponds to the thick black vertical line from the inner to the outer wall.

The divergent-free radial magnetic field satisfies

$$B_r(r) = B_{r_1} \frac{r_1}{r}, \qquad \text{(Eq. 1)}$$

with B_{r1} known. The induced magnetic field is neglected.
The 1Dr model considers a prescribed constant axial electric field E_z which does not accelerate the ions. Instead, macro-ions are inserted initially or created later with a mean axial velocity u_{zi}, and they are advanced only with the radial electric field. This procedure avoids refreshing of ions and electrons during the simulation, caused by the secular change of the ion axial velocity. The axial electric field affects electrons only, primarily by forcing with the magnetic field the electron $E \times B$ azimuthal drift. The radial electric field, $E_r = -d\phi/dr$, with $\phi(r, t)$ the electric potential, satisfies

$$\frac{\varepsilon_0}{r} \frac{\partial}{\partial r} \left(r \frac{\partial \phi}{\partial r} \right) = \rho_{el}(r, t), \qquad \text{(Eq. 2)}$$

with ρ_{el} the net electric charge density of the plasma, and the boundary conditions

$$\phi_2 = 0, \qquad \varepsilon_0 E_{r2} = -\sigma_2(t), \qquad \text{(Eq. 3)}$$

at the outer wall, $r = r_2$, where ε_0 is the vacuum permittivity and σ_2 is the surface charge there. It can then be shown that

$$\varepsilon_0 E_{r1} = \sigma_1(t), \qquad \text{(Eq. 4)}$$

with σ_1 the surface charge at $r = r_1$ is satisfied automatically.
The above surface charges are created by accumulation over time of the net normal electric current to the wall

$$\sigma_l(t) = -\int dt \boldsymbol{j}_l(t) \cdot \mathbf{1}_l, \quad l = 1, 2, \qquad \text{(Eq. 5)}$$

where $\boldsymbol{j}_l$ is the net electric current density to the wall and $\mathbf{1}_l$ is the wall normal pointing towards the plasma.
The collisional processes implemented in the code are: electron-neutral collisions, including elastic scattering, excitation and single ionization, following the models of Refs. [9–11]; and electron-ion, electron-electron and ion-ion Coulomb collisions, according to the models of Refs. [12–15].
Turning now to plasma-wall interaction, ions and electron reaching the radial walls are collected (formally); ion recombination is not considered explicitly since neutrals are modeled through a background density $n_n(t)$. The SEE produced by the impacting electrons follows the probabilistic model of Ref. [16], already implemented in Ref. [2]. The total SEE yield in that model accounts for elastically and inelastically backscattered electrons, and true secondary electrons (those extracted from the surface layers of the material), and thus may be expressed as

$$\delta_{SEE}(E) = \delta_{BS}(E) + \delta_{TS}(E) \qquad \text{(Eq. 6)}$$

where $\delta_{BS}(E)$ and $\delta_{TS}(E)$ stand for the total (i.e. elastic and inelastic) backscattering yield and the true secondary yield, respectively, with E the impacting electron energy.
Secondary electrons are transferred to the primary population when they undergo a collision with neutrals or a large angle (higher than 90 degrees) Coulomb collision. Three different electron species are considered hereafter: primary electrons p, and secondary electrons emitted by the inner $s1$ and outer $s2$ walls. Notice that, in a kinetic or particle formulation, this distinction between 'secondary' and 'primary' populations is just convenient for the analysis of the plasma response. On the contrary, that distinction acquires full sense in multi-fluid electron models.
The main model input parameters are listed on Tab. 1 for the different simulation cases. Xenon is the considered propellant. All electron and ion macroparticles have the same weight W (number of elementary particles per macroparticle) throughout the simulation, and the initial number of both electron and ion macroparticles is $N_{p0} \approx 10^5$, corresponding to about 70 macroparticles per cell. It has been checked that using the double number of particles per cell reduces only the PIC fluctuations, without changing the averaged trends.

Type	Description, symbol and units	Case 1	Changes from case 1
Populations settings	Number of elementary particles per macroparticle, W (-)	$3 \cdot 10^9$	-
	Initial average plasma density, n_{e0} (10^{17}m ^{3})	0.8	-
	Initial number of ions and electrons*, N_{p0} (-)	106814	-
	Initial electron temperature, T_{e0} (eV)	10	-
	Initial ion temperature, T_{i0} (eV)	1	-
	Ion axial mean velocity, u_{zi} (km/s)	10	-
	Initial background neutral density, n_{n0} (10^{17} m ^{3})	40	-
	Neutral temperature, T_n (K)	700	-
$\mathbf{E}$, $\mathbf{B}$ **fields**	Electric field axial component, E_z (V/cm)	100	Case 2: 200
	Magnetic field radial component at inner radius, B_{r_1} (G)	150	Case 2: 300
Simulation parameters	Backscattering SEE yield, $\delta_{BS}(E)$ (-)	OFF	Case 3: ON
	True secondary SEE yield, $\delta_{TS}(E)$ (-)	ON	-
	Walls temperature, T_{eW} (eV)	2	Case 4: 0.2
	Inner radius, r_1 (cm)	3.5	Case 5: 103.5
	Outer radius, r_2 (cm)	5.0	Case 5: 105.0
	Number of nodes, N_r (-)	1500	-
	Grid spacing*, Δr (m)	10	-
	Time step, Δt, (ps)	5	-
Physical parameters	Debye length*, λ_D (μm)	83.1	-
	Electron Larmor radius*, r_l (m)	802.0	Case 2: 401.0
	Inverse of plasma frequency*, $1/\omega_{pe}$ (ps)	62.7	-
	Inverse of electron cyclotron frequency*, $1/\omega_{ce}$, (ps)	379.1	Case 2: 189.5

Table 1: Main input parameters including initial population settings, externally applied fields and grid definition for the case 1 (reference case of Ref. [1]). The changes with respect to the case 1 defining the rest of the cases considered are indicated in the last column. The magnitudes marked with an asterisk (*) are not input parameters of the model, but are derived from the other parameters instead. The variables named as physical parameters are estimated from the other input values given at initial conditions.

Second order finite difference schemes are used for discretizing Poisson equation along the cylindrical radial coordinate r. The Thomas tridiagonal algorithm [17] is applied as direct solving technique. Once the radial electric field is updated, macroparticles are propagated along time using the Boris-Buneman leapfrog algorithm [18]. The time step is chosen so that $\Delta t < 0.3\omega_{pe}^{-1}$, where ω_{pe} is the plasma frequency. This condition ensures an accurate integration of the electron gyromotion since $\omega_{pe} > \omega_{ce}$, with ω_{ce} the electron gyrofrequency (see Tab. 1).

After advancing all macroparticles one time step, a Monte Carlo Collisions algorithm simulates the collisional events. A mean axial velocity u_{zi} is added to any new-born ion. More details on the algorithm and procedure can be found in [1]. Regarding the emission of true-secondary electrons, a zero-drift semi-Maxwellian distribution with temperature T_{eW} is assumed.

Plasma macroscopic properties are computed at the mesh nodes through the area weighting algorithm of Ref. [18] and the cylindrical correction of Ref. [19]. The extended volumetric weighting (EVW) algorithm of Ref. [1] is used to assess correctly the densities of minor species and higher-order moments (such as temperature) of all species. In a given node, the EVW defines the density, macroscopic velocity, and temperature of species $j = i, e$ as

$$n_j = \frac{W}{N_k \Delta V} \sum_k \sum_p s_p, \qquad \text{(Eq. 7)}$$

$$\boldsymbol{u}_e = \frac{\sum_k \sum_p \boldsymbol{v}_p s_p}{\sum_k \sum_p s_p}, \qquad \text{(Eq. 8)}$$

$$T_e = \frac{m_e}{3} \frac{\sum_k \sum_p |\boldsymbol{v}_p - \boldsymbol{u}_e|^2 s_p}{\sum_k \sum_p s_p}. \qquad \text{(Eq. 9)}$$

where ΔV is the weighting volume associated to the node, s_p is the linear weighting function assigning a weight to each macroparticle depending on its relative position and distance to the node, the sum in p is for all macroparticles with $s_p \neq 0$, and the sum in k is for N_k timesteps. Additionally, surface weighting schemes [20, 21] are used for updating the particle fluxes to the walls.

In general, new simulations are started assuming uniform Maxwellian populations of electrons and ions of the same density and a radially constant potential. In the first timesteps, this implies large electron currents to the walls. These build up negative surface charges there, which within 1μs create the Debye sheaths that confine electrons. The surface

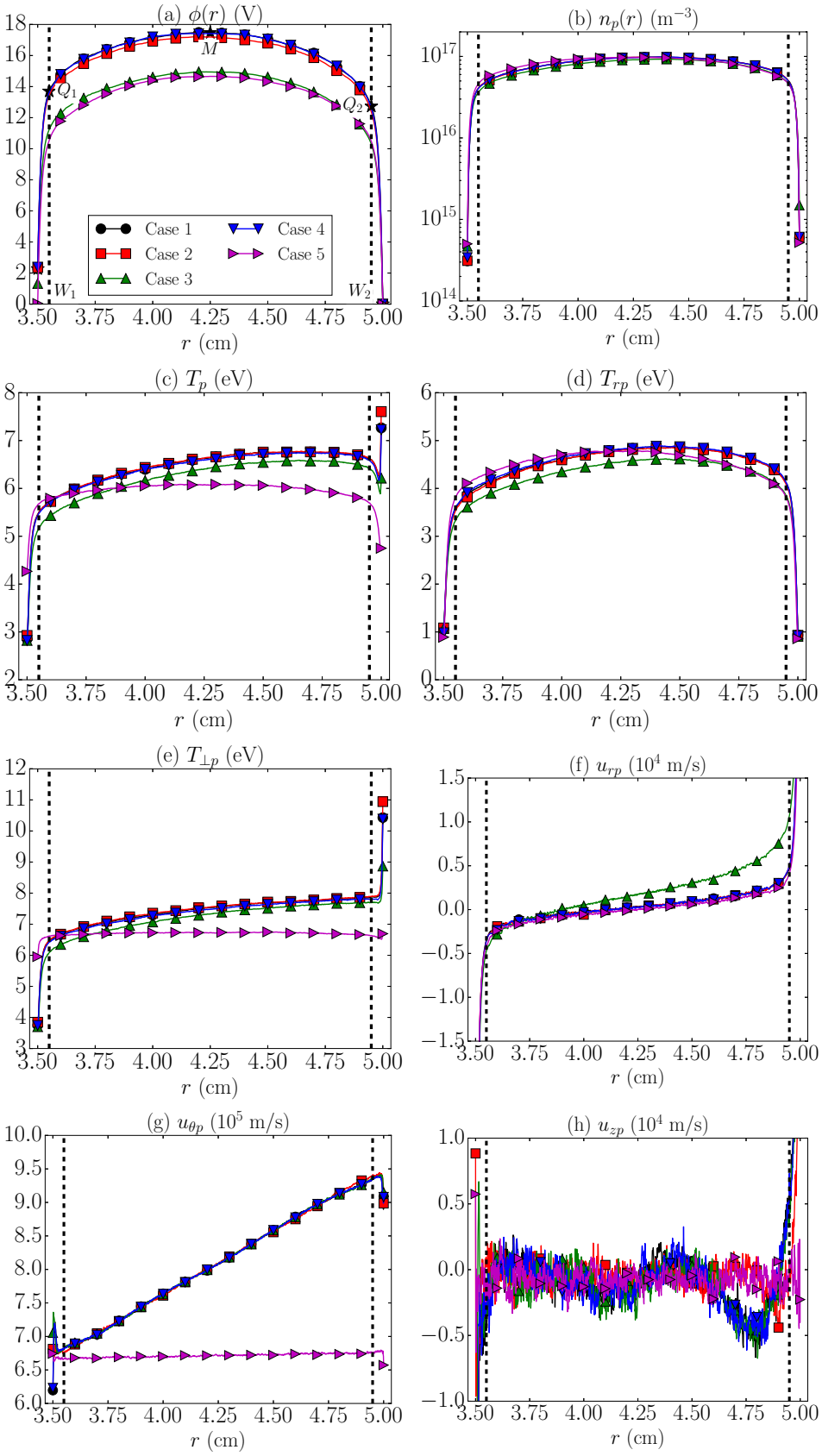

Figure 2: Steady-state radial profiles of different macroscopic magnitudes for primary electrons for the cases considered: (a) electric potential; (b) electron density; (c-e) electron total, parallel (radial) and perpendicular temperatures, respectively; (f-h) radial, azimuthal and axial electron mean velocities, respectively. Black stars on (a) indicates the points at the walls, sheath edges and channel mid radius. The weighted magnitudes are computed through the EVW algorithm with $N_k = 2 \cdot 10^5$ timesteps (equivalent to 1 s of simulation time).

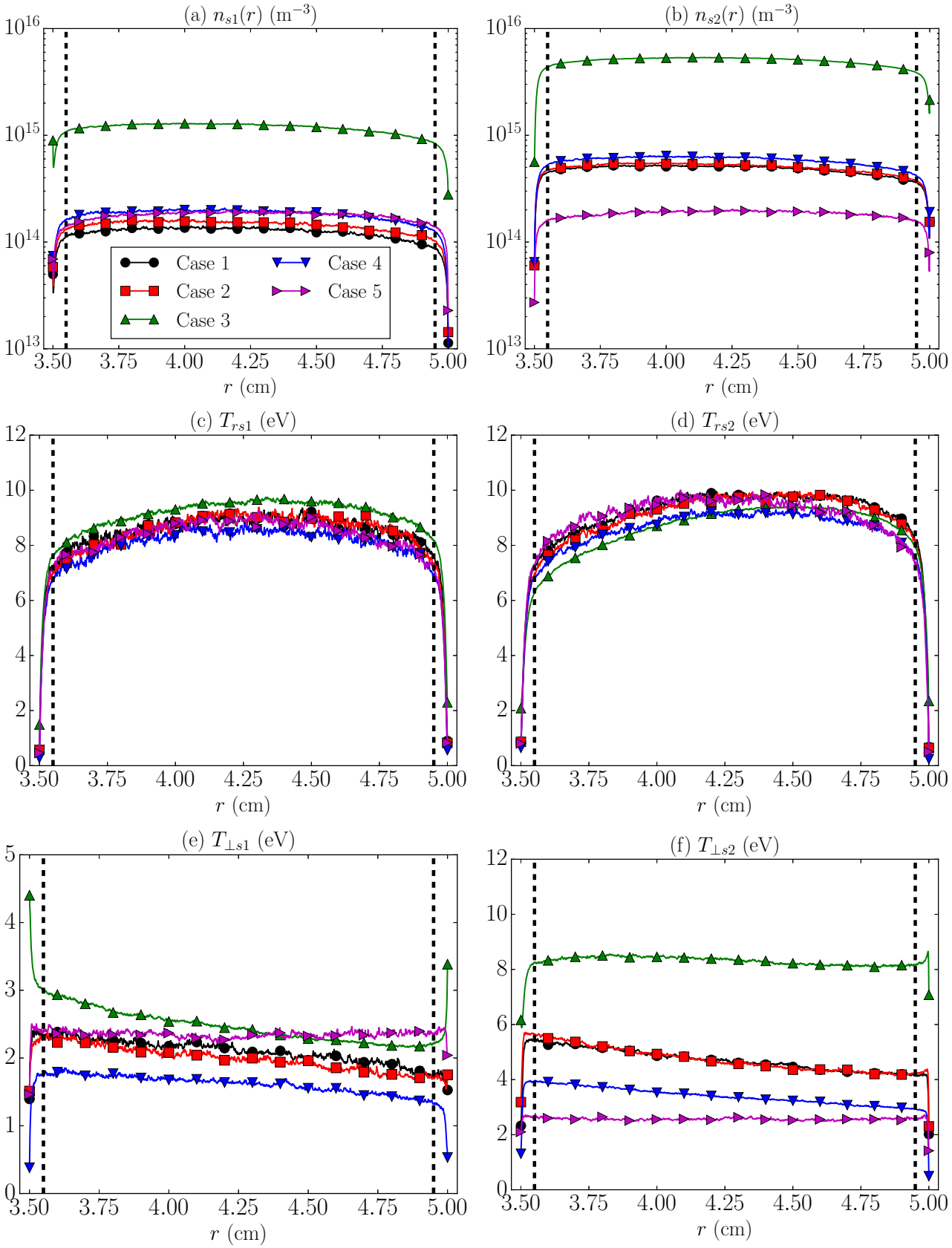

Figure 3: Steady-state radial profiles of different macroscopic magnitudes for secondary electrons for the cases considered: (a-b) electron density; (c-d) radial temperature; (e-f) perpendicular temperature, for $s1$ and $s2$ electron populations, respectively. The weighted magnitudes are computed through the EVW algorithm with $N_k = 2 \cdot 10^5$ timesteps (equivalent to 1 s of simulation time).

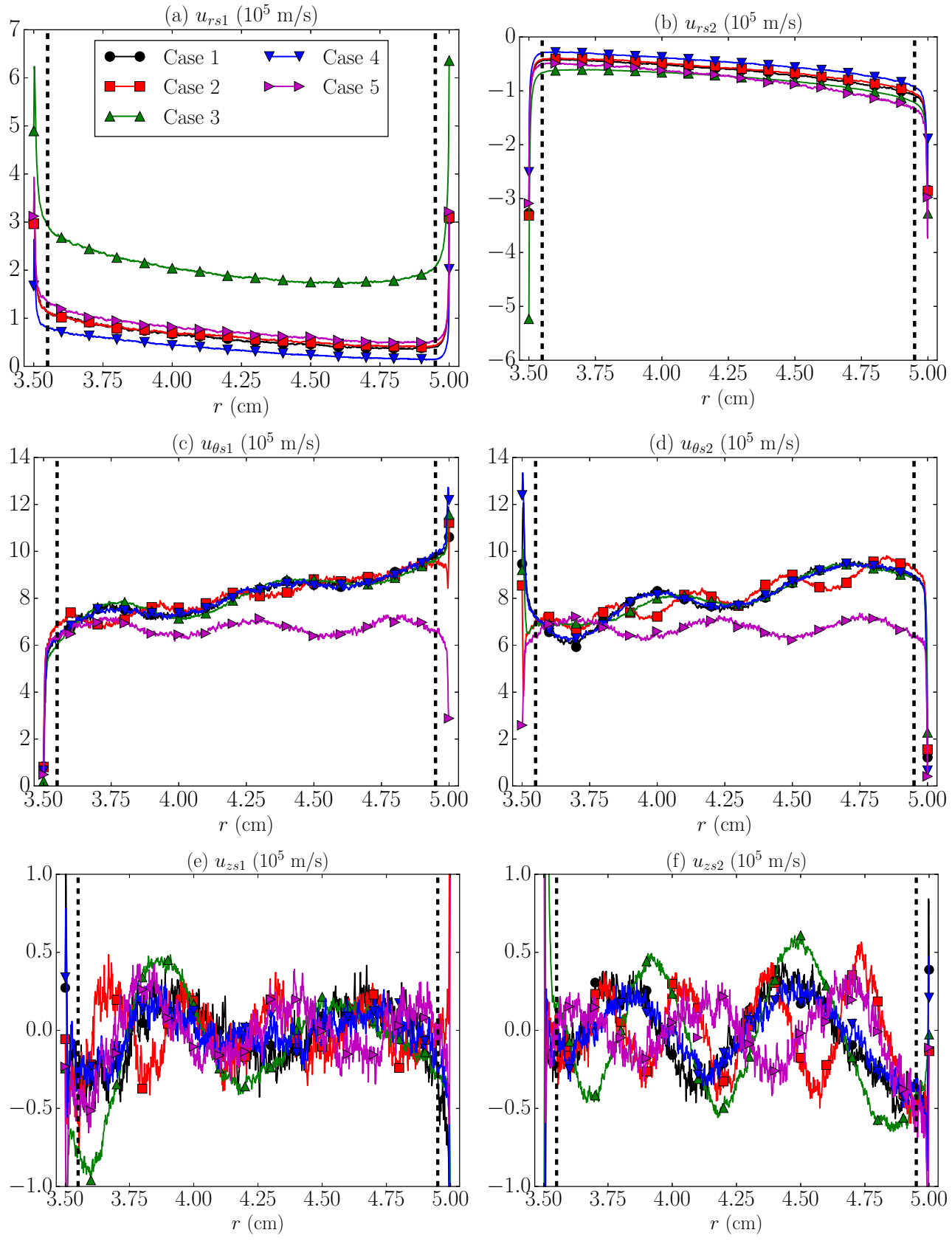

Figure 4: Steady-state radial profiles of macroscopic velocity components for secondary electrons for the cases considered: (a-b) radial velocity; (c-d) azimuthal velocity; (e-f) axial velocity, for $s1$ and $s2$ electron populations, respectively. The weighted magnitudes are computed through the EVW algorithm with $N_k = 2 \cdot 10^5$ timesteps (equivalent to 1 s of simulation time).

charges reach a steady state when the net electric currents to the walls become zero, [see Eq. (5)].

3. RESULTS

The stationary plasma discharge obtained for the 5 cases with main input parameters listed on Tab. 1 is analyzed in this section. The reference case, named here as case 1, corresponds to that analyzed in detail on Ref. [1]. The changes from the case 1 defining the rest of the cases considered in this work are indicated on Tab. 1. For all the of them, Tab. 2 summarizes relevant data of the corresponding discharge. Average values over 1 s of simulation time are considered. Figs. 2-4 show the radial profiles of the main plasma macroscopic magnitudes obtained through the EVW algorithm with $N_k = 2 \cdot 10^5$ timesteps (1 s of simulation time). For the sake of clarity, the offset in the radial coordinate of the case 5 is eliminated for plotting purposes. The vertical dashed lines in Figs. 2-4 represent approximately the edges of the Debye sheaths, which are located at 0.5mm from the walls, and where the radial ion Mach number is found to be approximately 1. The definition of 'sheath edges' in the present one-scale model is just meant for discussion purposes, since plasma response is known to change sharply when entering the thin Debye sheaths. The discussion here is focused on the plasma bulk.

The electric potential radial profiles are depicted on Fig. 2(a). Points W_1, W_2, Q_1, Q_2, and M correspond to walls, sheath edges, and channel mid radius, respectively. The electric potential values at those points is listed in Tab. 2. As already found on Ref. [1], the magnetic mirror effect and the centrifugal force in the cylindrical geometry lead to asymmetric radial profiles in the cases 1 to 4. The potential drop $\Delta\phi_{W_1W_2} > 0$ and the change on the $E \times B$ drift due to the radially varying magnetic field facilitate that electrons emitted from the wall W_2 be recollected at the wall W_1. On the contrary, the magnetic mirror effect opposes the electron collection at W_1. This asymmetry becomes also evident in the collected electron currents at the walls, in the mean wall impact energy per particle and thus in the SEE yields. All these data is detailed in Tab. 2 for each case considered. As expected, the asymmetry vanishes in the planar case (case 5), in which the effect of the geometric cylindrical expansion (i.e. terms $\sim 1/r$) tends to zero. This case will be further analyzed below. Tab. 2 also provides the fractions of secondary electrons recollected at each wall and transferred to the primary population through collisional processes. A significant secondary electron recollection at walls is found due to the low collisionallity regime. For all cases Coulomb collisions are negligible compared to electron-neutral collisions, but even the elastic e-n collision frequency, ~ 3.7MHz, is low compared with the transit frequency, ~ 62MHz. The SEE yields and the amounts of wall-recollection and thermalization determine the density and other macroscopic properties of secondary electrons.

Figs. 2(b), 3(a) and 3(b) plot the density profiles for p, $s1$ and $s2$ electrons, respectively, confirming the much lower density of the secondary electrons and thus their minor role in shaping the electric potential. The lower $s1$-density is partially caused by the lower SEE yield at the inner wall in all cases.

Figs. 2(c-e) show the total, radial (i.e. B-parallel) and perpendicular temperature profiles for the primary electrons population. Likewise, parallel and perpendicular temperatures profiles are depicted in Figs. 3(c) and 3(e) for the $s1$-electrons and in Figs. 3(d) and 3(f) for the $s2$-electrons. For the three populations, it is found $T_\theta \approx T_z \approx T_?$ and the anisotropy is the combined consequence of the electron magnetization and depletion at walls. The radial and perpendicular temperature values at point M are listed in Tab. 2 for each electron population. The ratio $T_r/T_?$ is lower than 1 for primary electrons and larger than 1 for secondary electrons in all cases considered but the case 3 for $s2$-electrons. This fact will be commented below. The temperature behavior of primary electrons is a direct consequence of the partial depletion of the radial VDF tail [1]. In general, p-electrons bounce radially between the sheaths several times before completing an azimuthal turn. The collisions (mainly with the neutral gas) introduce a larger dispersion (i.e. temperature) on the B-perpendicular direction and contribute to the replenishment of the primary EVDF tails. In contrast, the secondary electrons emitted from the walls are radially accelerated by the sheaths and act like two opposite radial beams before being quickly collected at the walls. The trend $T_r/T_? > 1$ is further enhanced by the fact that when they collide strongly (i.e electron-neutral or large angle Coulomb collisions) they are transferred to the primary population.

The macroscopic radial velocity profiles for the p, $s1$ and $s2$ electron populations are depicted in Figs. 2(f), 4(a) and 4(b), respectively. Primary electrons behave as usual with fluxes from the channel midpoint M to the walls. The velocity increase inside the sheaths is just the consequence of the decreasing density there. $s1$-electrons present a net outwards radial velocity, indicating that their outwards flow is slightly larger than the inwards one, due to a larger recollection at W_2. The opposite situation happens to $s2$-electrons.

The macroscopic azimuthal velocity of the three electron populations satisfy the $E \times B$ drift in all cases. The corresponding radial profiles for the p, $s1$ and $s2$ electrons are plotted in Figs. 2(g), 4(c) and 4(d), respectively. As it was already shown in Ref. [1], this result is particularly important to validate the simulation of the secondary electrons and reveals the excellent performance of the EVW algorithm in the computation of the weighted magnitudes

Type and units	Description and symbol	Case 1	Case 2	Case 3	Case 4	Case 5
Electric potentials (V)	At the mid radius M, ϕ_M	17.47	17.19	14.94	17.41	14.66
	At the inner sheath edge Q_1, ϕ_{Q_1}	13.70	13.44	11.24	13.62	10.53
	At the outer sheath edge Q_2, ϕ_{Q_2}	12.74	12.38	10.30	12.61	10.47
	At the inner wall W_1, ϕ_{W_1}	2.27	2.35	1.33	2.39	0.05
	At the outer wall W_2, ϕ_{W_2}	0.00	0.00	0.00	0.00	0.00
Current densities (A/m^2)	p to the inner wall, $\lvert j_{p,1} \rvert$	12.80	13.19	20.99	13.62	17.88
	$s1$ to the inner wall, $\lvert j_{s1,1} \rvert$	0.17	0.21	1.81	0.29	0.17
	$s1$ from the inner wall, $\lvert j_{s1,1+} \rvert$	2.36	2.75	54.08	2.51	3.35
	$s2$ to the inner wall, $\lvert j_{s2,1} \rvert$	2.96	2.93	44.90	2.26	1.20
	p to the outer wall, $\lvert j_{p,2+} \rvert$	23.97	23.71	67.86	23.98	18.12
	$s1$ to the outer wall, $\lvert j_{s1,2+} \rvert$	0.48	0.64	26.95	0.22	1.05
	$s2$ to the outer wall, $\lvert j_{s2,2+} \rvert$	0.81	0.71	29.17	0.54	0.20
	$s2$ from the outer wall, $\lvert j_{s2,2} \rvert$	7.23	7.17	106.31	6.94	3.53
Mean impact energies per elementary particle (eV)	e at the inner wall, $E_{we,1}$	8.10	8.72	12.36	8.04	9.35
	p at the inner wall, $E_{wp,1}$	8.50	9.01	8.49	6.87	9.71
	$s1$ at the inner wall, $E_{ws1,1}$	4.06	4.08	3.78	3.86	3.79
	$s2$ at the inner wall, $E_{ws2,1}$	6.59	7.76	14.52	7.25	4.76
	e at the outer wall, $E_{e,2}$	15.75	15.99	14.99	15.74	9.64
	p at the outer wall, $E_{wp,2}$	16.16	16.36	13.90	16.07	9.99
	$s1$ at the outer wall, $E_{ws1,2}$	6.24	8.11	13.90	5.55	4.75
	$s2$ at the outer wall, $E_{ws2,2}$	9.34	10.94	18.54	5.13	3.91
SEE yields (-)	Backscattering at the inner wall, $\delta_{BS,1}$	0.00	0.00	0.57	0.00	0.00
	True secondary at the inner wall, $\delta_{TS,1}$	0.15	0.17	0.23	0.16	0.17
	Backscattering at the outer wall, $\delta_{BS,2}$	0.00	0.00	0.58	0.00	0.00
	True secondary at the outer wall, $\delta_{TS,2}$	0.29	0.29	0.27	0.28	0.18
Conversion to p and wall collection fractions (%)	$s1$ conversion to p	63.2	59.1	25.4	76.2	63.2
	$s1$ collection at the inner wall	7.5	7.8	3.4	11.5	4.9
	$s1$ collection at the outer wall	29.3	33.1	71.2	12.3	31.9
	$s2$ conversion to p	60.1	61.4	43.0	69.4	60.7
	$s2$ collection at the inner wall	28.7	28.6	29.6	22.8	33.6
	$s2$ collection at the outer wall	11.2	10.0	27.0	7.8	5.7
Electron temperatures at M (eV)	p radial, $T_{rp,M}$	4.81	4.80	4.55	4.83	4.77
	p perpendicular, $T_{?p,M}$	7.53	7.55	7.33	7.48	6.73
	$s1$ radial, $T_{rs1,M}$	8.97	9.07	9.55	8.45	8.88
	$s1$ perpendicular, $T_{?s1,M}$	2.06	2.01	2.45	1.64	2.30
	$s2$ radial, $T_{rs2,M}$	9.77	9.83	9.23	9.13	9.53
	$s2$ perpendicular, $T_{?s2,M}$	4.70	4.59	8.40	3.36	2.62

Table 2: Main parameters characterizing the steady-state discharge for the different cases considered. Time-averaged values over 1 s of simulation time are considered.

for the low-populated species.

Figs. 2(h), 4(e) and 4(f) show the profiles of the macroscopic axial velocity for the p, $s1$ and $s2$ populations, respectively. These velocities are close to zero except for the oscillations shown in secondary electrons which correspond to the well known near wall conductivity (NWC) phenomenon [22]. As proved in Ref. [1], the simulations confirm that there are not secular effects on the axial flow of all populations and therefore there is no need of performing particle refreshing.

After describing the general structure of the plasma discharge in all cases considered, in the following some particularities of the cases 2 to 5 are worth to be commented in comparison to the reference case 1.

Regarding the case 2, when both the axial electric field and the radial magnetic field are doubled, the number of peaks in the secondary electrons azimuthal and axial macroscopic velocity profiles is doubled (see Figs 4(d) and 4(f) for the $s2$-electrons, for example) while the rest of plasma properties (including the electric potential and the electron temperatures) remain the same, as expected.

In the case 3 we have considerably larger total SEE yields: ~ 0.8 and ~ 0.85 at the inner and outer walls, respectively. As listed in Tab. 2, $\delta_{BS} > \delta_{TS}$, which is consistent with the SEE analysis performed in Ref. [2] for the impacting energy values obtained in this case. As a result, the sheaths potential drops

decrease by a value of ~ 1.5eV and of ~ 2.5eV at the inner and outer walls, respectively, thus facilitating the electron collection at the walls both for primary and secondary electrons. Consequently, larger electron current densities to the walls are obtained and, since the collisional frequencies remain approximately the same, the secondary electrons wall collection fractions increase (see values in Tab. 2). This physical argument could explain the slightly lower primary electron temperatures obtained [see Figs. 2(c-e)], and the fact that the ratio $T_r/T_?$ becomes smaller than 1 for $s2$-electrons in the region from $r \approx 3.9$cm to the inner wall.

In the case 4 secondary electrons are emitted with 10 times less energy due to the lower wall temperature. As expected, they exhibit lower temperatures and lower absolute values of the macroscopic radial velocity. The influence of the wall temperature in the rest of plasma radial profiles is negligible. Due to their lower energy, secondary electrons spend a longer time bouncing radially between the sheaths where an eventual collision may turn them into the primary population. This explains the significantly larger thermalization fractions of both the $s1$ and $s2$ electrons (see Tab. 2).

Finally, special attention must be paid to the case 5. As mentioned above, the typical geometrical effects in cylindrical coordinates (i.e. terms $\sim 1/r$) become negligible when the simulation domain is displaced towards larger radii (e.g. 1m displacement in the case 5). Therefore, the case 5 corresponds to a planar simulation in which the applied radial magnetic field is approximately constant (from Eq. (1): $B_{r_2}/B_{r_1} = r_1/r_2 = 0.986 \sim 1$). Hence, the $E \times B$ drift is approximately constant as well, and the magnetic mirror effect becomes negligible along the simulation domain. As a result, the asymmetries in the radial profiles and in the different magnitudes at the walls vanish. Interestingly, the different electron populations exhibit a similar temperature anisotropy in comparison to the other cases.

Neglecting collisions, the macroscopic radial equilibrium for p electrons integrated along the radial coordinate yields

$$(e\phi - e\phi_M) - T_{rpM} \ln \frac{n_p}{n_{pM}} = (T_{rp} - T_{rpM}) + \int_{r_M}^{r} dr\, (T_{rp} - T_{rpM}) \frac{d \ln n_p}{dr} + \int_{r_M}^{r} dr \frac{T_{rp} - T_{?p}}{r} - \int_{r_M}^{r} dr \frac{m_e u_{\theta p}^2}{r}. \quad \text{(Eq. 10)}$$

The left side of Eq. (10) groups the terms of the Boltzmann relation while the right side groups all terms (the non-uniform radial temperature, the magnetic mirror effect, which in turn is a combination of temperature anisotropy and cylindrical expansion, and the centrifugal force) affecting their fulfillment. The results shown in Ref. [1] for the case 1 are here compared to those of the case 5 in Fig. (5). The whole radial equilibrium of Eq. (10) is excellently satisfied in both cases confirming the marginal role of the collisional processes and other convection effects. In the case 1, the three terms of the right side of Eq. (10) are of the same order and the sum of these 3 contributions introduces a correction of up to 30% (relative to $e\phi - e\phi_M$) in the Boltzmann relation. In the case 5 however, the terms $\sim 1/r$ vanish so that the correction below reduces approximately up to 15% and is mostly due to the non-uniform radial temperature.

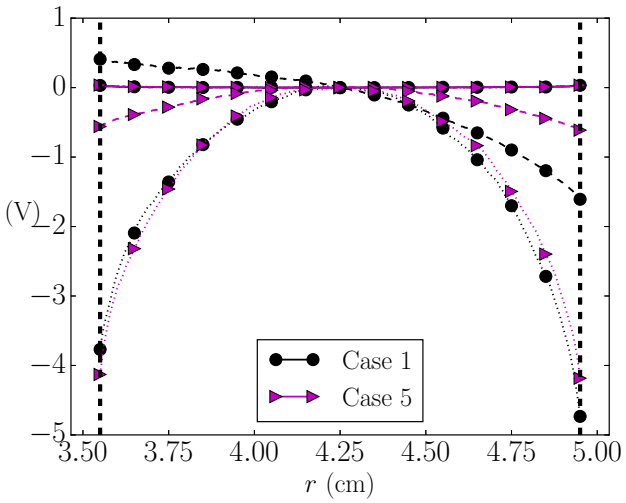

Figure 5: Fulfilment of the integrated radial momentum balance of electrons in Eq. (10) (solid lines); Boltzmann relation (dashed lines); electric potential profile relative to ϕ_M (dotted lines). Dashed vertical lines mark approximate sheath edges location. The macroscopic variables involved are computed through the EVW algorithm with $N_k = 2 \cdot 10^5$ timesteps (equivalent to 1 s of simulation time).

4. CONCLUSIONS

This work advances in the previous investigation carried out in Ref. [1] simulating a steady HET plasma discharge in different scenarios and analyzing the effect of different parameters in order to get a further insight of the discharge structure. The annular model and related PIC/MCC code of given axial section of the acceleration region of a HET was built on a previous one by Taccogna [2]. Important improvements have been recently added [1]. The main concluisions are the following. The case 2 allows the further code validation specially for what concerns the simulation of the dynamics of the secondary electron populations: the number of turns along the radial coordinate doubles when both the electric and the magnetic field are doubled while keeping the same electron temperature. The case 3 explores the influence of a complete SEE including

backscattered electrons. The total SEE yields are found to be significantly larger with a predominance of the backscattering process. The enhanced SEE reduces the sheath potential drops which facilitates the electron wall collection. This could explain the primary electron population temperature decrease in the bulk plasma. The influence of the wall temperature for the SEE has a negligible effect on the structure of the plasma discharge, as illustrated by the case 4. Finally, as expected, the cylindrical effects inducing asymmetries in the macroscopic profiles and in the different plasma magnitudes at the inner and outer walls vanish in the planar case 5. However, the electron temperature anisotropy induced by the magnetic field follows the same trend as in the reference case 1. From the analysis of the radial momentum equilibrium for the primary electron population, a smaller deviation from the Boltzmann relation is found in this case since the influence of the magnetic mirror effect (which is a combination of temperature anisotropy and cylindrical divergence) and the centrifugal force tends to zero as $1/r$.
Further work will focus on the effect of a higher axial electric field in the reported transition from a stationary solution to an instability saturated one. In addition, a non-purely radial magnetic field should change substantially the plasma discharge structure and thus have important consequences on the electron VDFs.

5. ACKNOWLEDGMENTS

The work at UC3M was supported by the CHEOPS project, funded by the European Union's Horizon 2020 Research and Innovation Programme, under Grant Agreement 730135. Additional support came from the Spain´s National Research and Development Plan (Project ESP2016-75887). F. T. was supported by the ApuliaSpace Project (grant PON03PE_00067_6).

6. REFERENCES

[1] Domínguez-Vázquez, A., Taccogna, F., and Ahedo, E., "Particle modeling of radial electron dynamics in a controlled discharge on a Hall thruster," *Plasma Sources Science and Technology*, 2018, Submitted.

[2] Taccogna, F., Longo, S., Capitelli, M., and Schneider, R., "Surface-driven asymmetry and instability in the acceleration region of a Hall thruster," *Contrib. Plasma Phys.*, Vol. 48, No. 4, 2008, pp. 1–12.

[3] Ahedo, E. and Parra, F. I., "Partial trapping of secondary electron emission in a Hall thruster plasma," *Physics of Plasmas*, Vol. 12, No. 7, 2005, pp. 073503.

[4] Ahedo, E. and Pablo, V. d., "Combined effects of electron partial thermalization and secondary emission in Hall thruster discharges," *Physics of Plasmas*, Vol. 14, 2007, pp. 083501.

[5] Sydorenko, D., Smolyakov, A., Kaganovich, I., and Raitses, Y., "Modification of electron velocity distribution in bounded plasmas by secondary electron emission," *Plasma Science, IEEE Transactions on*, Vol. 34, No. 3, 2006, pp. 815–824.

[6] Kaganovich, I. D., Raitses, Y., Sydorenko, D., and Smolyakov, A., "Kinetic effects in a Hall thruster discharge," *Phys. Plasmas*, Vol. 14, No. 5, 2007, pp. 057104.

[7] Taccogna, F., Longo, S., Capitelli, M., and Schneider, R., "Particle-in-Cell Simulation of Stationary Plasma Thruster," *Contributions to Plasma Physics*, Vol. 47, No. 8-9, 2007, pp. 635–656.

[8] Taccogna, F., Schneider, R., Longo, S., and Capitelli, M., "Kinetic simulations of a plasma thruster," *Plasma Sources Sci. Technol.*, Vol. 17, No. 2, 2008, pp. 024003.

[9] Nanbu, K., "Probability theory of electron-molecule, ion-molecule, molecule-molecule, and Coulomb collisions for particle modeling of materials processing plasmas and gases," *Trans. Plasma Sci.*, Vol. 28, No. 3, 2000, pp. 971–990.

[10] Nanbu, K., "Simple method to determine collisional event in Monte Carlo simulation of electron-molecule collision," *Jpn. J. Appl. Phys.*, Vol. 33, No. 8, 2000, pp. 4752–4753.

[11] Surendra, M., Graves, D. B., and Morey, I. J., "Electron heating in low-pressure rf glow discharges," *Appl. Phys. Lett.*, Vol. 56, No. 11, 1990, pp. 1022–1024.

[12] Nanbu, K., "Theory of cumulative small-angle collisions in plasmas," *Phys. Rev. E*, Vol. 55, No. 4, 1997, pp. 4642–4652.

[13] Nanbu, K. and Yonemura, S., "Weighted particles in Coulomb collision simulations based on the theory of a cumulative scattering angle," *J. Comput. Phys.*, Vol. 145, 1998, pp. 639–654.

[14] Bobylev, A. V. and Nanbu, K., "Theory of collision algorithms for gases and plasmas based on the Boltzmann equation and the Landau-Fokker-Plack equation," *Phys. Rev. E*, Vol. 61, No. 4, 2000, pp. 4576–4586.

[15] Wang, C., Lin, T., Caflisch, R., Cohen, B. I., and Dimits, A. M., "Particle simulation of Coulomb collisions: comparing the methods of Takizuka & Abe and Nanbu," *J. Comput. Phys.*, Vol. 227, 2008, pp. 4308–4329.

[16] Furman, M. A. and Pivi, M. T. F., "Probabilistic model for the simulation of secondary electron emission," *Phys. Rev ST Accel. Beams*, Vol. 5, No. 12, 2002, pp. 124404.

[17] Press, W. H., Teukolsky, S. A., Vetterling, W. T., and Flannery, B. P., *Numerical recipes in Fortran 77: the art of scientific computing*, Cambridge University Press, New York, 2001, Available online: http://numerical.recipes/.

[18] Birdsall, C. K. and Langdon, A. B., *Plasma physics via computer simulation*, Adam Hilger, Bristol, Philadelphia and New York, 1991.

[19] Verboncoeur, J. P., "Symmetric spline weighting for charge and current density in particle simulation," *Journal of Computational Physics*, Vol. 174, 2001, pp. 421–427.

[20] Santos, R., Ahedo, E., and Santos, R., "Implementation of the kinetic Bohm condition in a Hall thruster hybrid code," *45th AIAA/ASME/SAE/ASEE Joint Propulsion Conference & Exhibit*, 2009, p. 4913.

[21] Ahedo, E., Santos, R., and Parra, F. I., "Fulfillment of the kinetic Bohm criterion in a quasineutral particle-in-cell model," *Physics of Plasmas*, Vol. 17, No. 7, 2010, pp. 073507.

[22] Bugrova, A., Morozov, A. I., and Kharchevnikov, V. K., "Experimental studies of near wall conductivity," *Fizika Plazmy*, Vol. 16, No. 12, 1990, pp. 1469–1481.